tron irradiation–induced defects, impurities, or oxygen vacancies) and correlated defects (for example, twin boundaries or columnar defects generated by heavy-ion irradiation). The former is effective at low temperature, whereas the latter plays a crucial role at high temperature.
8. L. Civale *et al.*, *Phys. Rev. Lett.* **67**, 648 (1991).
9. M. Konczykowski *et al.*, *Phys. Rev. B* **44**, 7167 (1991).
10. J. R. Thompson *et al.*, *Appl. Phys. Lett.* **60**, 2306 (1992).
11. W. Gerhauser *et al.*, *Phys. Rev. Lett.* **68**, 879 (1992).
12. H. Kumakura *et al.*, *J. Appl. Phys.* **74**, 451 (1993).
13. A. K. Pradhan *et al.*, *Phys. Rev. B* **53**, 2269 (1996).
14. P. Yang and C. M. Lieber, *Science* **273**, 1836 (1996).
15. M. Takano *et al.*, *Jpn. J. Appl. Phys.* **27**, L1041 (1988).
16. N. Fukushima *et al.*, *Physica C* **159**, 777 (1989).
17. Y. Ikeda *et al.*, *ibid.* **165**, 189 (1989).
18. P. Majewski, S. Kaesche, H.-L. Su, F. Alginger, *ibid.* **221**, 295 (1994).
19. H. Ito, Y. Ikeda, Z. Hiroi, M. Takano, Y. Bando, *J. Jpn. Soc. Powder Powder Metallurgy* **38**, 171 (1991).
20. T. Mochiku, in *Bismuth-Based High-Temperature Superconductors* (Dekker, New York, 1996), p. 227–237.
21. P. Fournier, A. Kapitulnik, A. F. Marshall, *Physica C* **257**, 291 (1996).
22. P. L. Gammel, L. F. Schnemeyer, J. V. Waszczak, D. J. Bishop, *Phys. Rev. Lett.* **61**, 1666 (1988).
23. C. P. Bean, *Rev. Mod. Phys.* **36**, 31 (1964).
24. Y. Matsui, H. Maeda, Y. Tanaka, S. Horiuchi, *Jpn. J. Appl. Phys.* **27**, L361 (1988).
25. J. L. Tallon, R. G. Buckley, P. W. Gilberd, M. R. Presland, *Physica C* **158**, 247 (1989).
26. D. J. Werder, C. H. Chen, S. Jin, R. C. Sherwood, *J. Mater. Res.* **4**, 748 (1989).
27. For the $x = 0.4$ crystal, about 10 fragments were examined in a microscope, and only one fragment exhibited a microstructure similar to that found in the $x = 0.6$ crystal. However, the domains in the $x = 0.4$ crystal were much smaller along the *a* axis (a few tens of nanometers) and were connected to each other to form meandering strings around the *a* axis.
28. Recently, cross-sectional HREM observations with an incident beam parallel to the *a* axis were performed on the $x = 0.6$ crystal. The results indicated that the typical length of the modulation-free domains along the *c* axis is a few micrometers, which means that the domains have a thin, platelike shape.
29. G. Yang *et al.*, *Phys. Rev. B* **48**, 4054 (1993).
30. R. Kleiner and P. Müller, *ibid.* **49**, 1327 (1994).
31. The relation between anisotropy and hole doping has been studied systematically in various HTSCs [K. Kishio *et al.*, *Physica C* **235**, 2775 (1994)]. With increasing hole-carrier density the anisotropy decreases, and thus B_{irr} increases.
32. It would be important to measure the angular dependence of pinning forces, because the domains have an anisotropic shape within the basal plane. The largest flux pinning should occur when the applied magnetic field is perpendicular to the *b* axis.
33. J. Shimoyama *et al.*, in preparation.
34. Recently, we detected a significant difference in the Pb content by using analytical electron microscopy.
35. The situation may be similar to that in the twin boundary in $YBa_2Cu_3O_{7-\delta}$, where the coherence length may be reduced due to electron scattering.
36. K. Kadowaki, in *4th International Symposium on Superconductivity (ISS '91), Tokyo*, H. Hayakawa and N. Koshizuka, Eds. (Springer Verlag, Tokyo, 1991), pp. 395–400.
37. We thank Y. Matsuda (Hokkaido University) for reviewing the manuscript and Rigaku Industrial Corporation for help with the fluorescence x-ray composition analysis. Supported in part by CREST (Core Research for Evolutional Science and Technology) of Japan Science and Technology Corporation (JST) and by the Original Industrial Technology R&D Promotion Program from the New Energy and Industrial Technology Development Organization (NEDO) of Japan.

31 December 1996; accepted 10 March 1997

High-Power Infrared (8-Micrometer Wavelength) Superlattice Lasers

Gaetano Scamarcio,* Federico Capasso,† Carlo Sirtori,‡ Jerome Faist, Albert L. Hutchinson, Deborah L. Sivco, Alfred Y. Cho

A quantum-cascade long-wavelength infrared laser based on superlattice active regions has been demonstrated. In this source, electrons injected by tunneling emit photons corresponding to the energy gap (minigap) between two superlattice conduction bands (minibands). A distinctive design feature is the high oscillator strength of the optical transition. Pulsed operation at a wavelength of about 8 micrometers with peak powers ranging from ~0.80 watt at 80 kelvin to 0.2 watt at 200 kelvin has been demonstrated in a superlattice with 1-nanometer-thick AlInAs barriers and 4.3-nanometer-thick GaInAs quantum wells grown by molecular beam epitaxy. These results demonstrate the potential of strongly coupled superlattices as infrared laser materials for high-power sources in which the wavelength can be tailored by design.

Semiconductor superlattices consist of a periodic stack of nanometer-thick layers of two materials (quantum wells and barriers) (*1*). The period *d* of this artificial crystal is typically much larger (~5 nm) than the lattice constant of the bulk crystalline constituents (~0.5 nm). This superimposed potential splits the conduction and valence bands in a series of much narrower bands (typically tens to a few hundred millielectron volts wide in the strong tunnel-coupling regime) called minibands, which are separated by energy gaps ("minigaps") along the direction normal to the layers (*1*). For a given choice of materials, miniband and minigap widths can be engineered by suitable choice of the layer's thickness, which can be atomically controlled with the use of thin-film crystal growth techniques such as molecular beam epitaxy (MBE) (*2*).

Although quantum wells, characterized by discrete energy levels caused by quantum confinement, have found wide use in semiconductor lasers for optical communications and optical recording and in other optoelectronic applications (*3*), the use of superlattices in optical devices has been limited. In their pioneering paper (*1*), Esaki and Tsu proposed their use as sources of submillimeter-wavelength coherent radiation emitted by electrons oscillating in phase in a high electric field normal to the layers (Bloch oscillations). This emission was recently observed (*4*) but is intrinsically of low power, and the goal of realizing an electrically pumped Bloch oscillator remains elusive.

We report a coherent infrared (IR) source based on strongly coupled superlattices that demonstrates the potential of these materials for lasers in the technologically important mid-IR spectrum. Laser action has been achieved between minibands through unipolar (electron) injection by interminiband tunneling. In our structure (Fig. 1), the laser transition is between states at the bottom of the second conduction miniband and empty states near the top of the first miniband at a photon energy well below the energy band gap of the barrier and well materials. The wavelength is thus determined by the minigap and can be selected in a large region of the IR spectrum by changing the barrier and well thickness. In the present structure, the wavelength λ was selected at $\cong 8$ μm, with the use of an eight-period superlattice with 1-nm-thick $Al_{0.48}In_{0.52}As$ barriers and 4.3-nm-thick $Ga_{0.47}In_{0.53}As$ quantum wells (*5*).

A distinctive design feature of this laser is the high oscillator strength of the direct optical transition at the mini–Brillouin zone boundary of the superlattice (Fig. 1B). The oscillator strength of radiative transitions between the first two minibands of a superlattice strongly increases with wave vector k_z as the barrier thickness is decreased and is maximum at the zone boundary ($k_z = \pi/d$) (*6*). For example, in our superlattice the ratio of oscillator strengths at $k_z = \pi/d$ and $k_z = 0$ is ~60, largely because of the variation of the transition matrix element z_{21} across the mini–Brillouin zone. By appropriately tailoring the barrier and well thickness, we optimized the structure for maximum oscillator strength (*6*) $f_{21} = (2m_0/\hbar^2)\hbar\omega z_{21}^2 = 55.4$ at $k_z = \pi/d$—where m_0 is the free electron mass and

Bell Laboratories, Lucent Technologies, 700 Mountain Avenue, Murray Hill, NJ 07974, USA.

*Present address: Dipartimento di Fisica, Università di Bari, 70126 Bari, Italy. E-mail: scamarcio@ba.infn.it
†To whom correspondence should be addressed. E-mail: fc@bell-labs.com
‡Present address: LCR Thomson-CSF, Domaine de Corbeville, 91400 Orsay, France.

$\hbar$ is Planck's constant divided by 2π—corresponding to a matrix element z_{21} = 3.6 nm at the designed photon energy (160 meV). This large value is an important factor in achieving the threshold gain at reasonable current densities. We have studied interminiband transitions in detail by performing electroluminescence (EL) experiments below threshold in a structure (sample D2173) with identical superlattice active regions and in two other AlInAs/GaInAs samples (D2135 and D2145) with different values of the minigap (251 and 162 meV, respectively), using the same injection scheme (*7*). The EL spectrum is dominated by optical transitions at the zone boundary even for injection well above the bottom of the upper miniband. This predominance is attributed to the ultrafast intraminiband relaxation ($\leq$1 ps) by emission of optical phonons (*8*) and the high matrix element of the zone-boundary optical transition.

Population inversion is automatically ensured because the lifetime $\tau_1 \approx 0.1$ ps of an electron at the top of the first miniband (*8*) is negligible with respect to the electron scattering time $\tau_{21} \approx 10$ ps by optical phonon emission from the bottom of the second miniband to the first miniband (*9*). This large difference is explained by the much greater momentum transfer for interminiband optical emission processes compared to intraminiband ones.

The present cascade configuration is similar to that previously used in intersubband quantum cascade (QC) lasers (*10*, *11*). Both lasers are unipolar, rather than relying on the bipolar injection and recombination of electrons and valence-band holes. However, the present laser differs in a fundamental way in the design of the active region. In the subband QC lasers, the optical transition is between discrete levels (subbands) of double (*10*) or single (*11*) quantum wells rather than between broad minibands of strongly coupled superlattices. This difference has important implications for the nature of the optical transition and for population inversion and injection. In intersubband QC lasers, population inversion is obtained by careful design of electronic states and scattering rates; in particular, resonant optical phonon emission between two closely spaced energy levels is used to minimize the lifetime of the lower state of the laser transition (*9*). In the present superlattice lasers, this lifetime is controlled by intraminiband phonon emission and is inherently ultrafast. For emission wavelengths in the mid-IR range (4 to 13 μm), it is always much shorter than the interminiband scattering time. Thus, the population-inversion condition is much less sensitive to the wavelength, simplifying the design of the laser. Finally, in QC lasers, injection is by resonant tunneling into an excited subband of a double well, whereas in the present device, injection is by interminiband tunneling (Fig. 1A). The high current carrying capability of wide minibands (>100 meV) combined with high injection efficiency are advantageous for achieving high peak power levels, a fact confirmed by our initial experiments. On the other hand, the peak of the interminiband EL spectrum is considerably broader (~30 meV at $\lambda \cong 8$ μm) than the intersubband EL spectrum of QC laser structures (~10 meV at $\lambda \cong 8$ μm), which results in higher threshold current densities, despite the larger transition matrix element.

The laser structure (Fig. 2) was grown by MBE with the $Al_{0.48}In_{0.52}As/Ga_{0.47}In_{0.52}As$ heterojunction material system lattice-matched to InP. Electrons are injected by tunneling into the second miniband of *n*-type–doped superlattice active regions alternated with doped injectors. This cascade configuration allows us to re-inject electrons into the adjacent active region after they have exited the preceding period. The many periods (N_p = 25) enhance the overlap factor between the fundamental mode of the optical waveguide and its core (superlattice active regions plus the injectors), increasing the modal gain of the laser. The slope efficiency (ratio of the laser output power to the difference between the laser and threshold currents) of the laser is also enhanced by the cascade configuration because it is proportional to N_p (*10*).

The choice of carrier concentration in the uniformly doped superlattice active regions ($n = 1 \times 10^{17}$ cm^{-3}) is important and is determined by several trade-offs. The

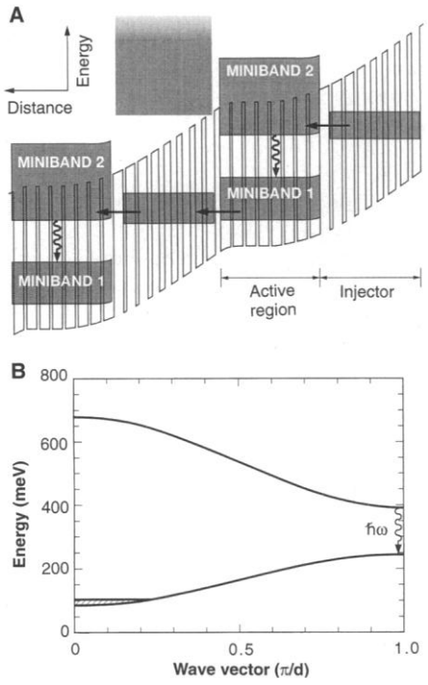

Fig. 1. (**A**) Calculated conduction band diagram of two stages of the 25-period (active regions and injector) superlattice laser. Electrons are injected by tunneling into the second miniband of *n*-type–doped superlattice active regions. These have 1-nm-thick $Al_{0.48}In_{0.52}As$ barriers and 4.3-nm-thick $Ga_{0.47}In_{0.53}As$ wells. Laser action (wavy arrow) occurs at the energy gap (minigap) between filled electronic states at the bottom of the second miniband and empty states at the top of the first miniband. The digitally graded AlInGaAs injectors consist of short-period *n*-type–doped AlInAs/GaInAs superlattices with varying duty cycle. (**B**) Calculated dispersion of the first two minibands of the superlattice active regions in the reduced Brillouin zone scheme. The wave vector k_z along the direction perpendicular to the layers is in units of the value at the mini–zone boundary ($k_z = \pi/d$), where d is the superlattice period (5.3 nm). The calculated widths of minibands 1 and 2 are Δ_1 = 146 meV and Δ_2 = 300 meV, respectively. The high–oscillator strength direct optical transition (wavy arrow) at the mini–zone boundary corresponds to a laser photon energy equal to the minigap (E_{mg} = 159 meV). The shaded area represents the range of occupied electronic states (Fermi energy) in the first miniband.

	n (cm^{-3})	Thickness (nm)	
GaInAs Sn doped	1.0×10^{20}	20.0	Contact layer
GaInAs	8.0×10^{18}	600.0	Waveguide cladding
AlGaInAs graded	5.0×10^{17}	40.0	
AlInAs	5.0×10^{17}	20.0	
AlInAs	3.0×10^{17}	1200.0	
AlInAs	1.2×10^{17}	1200.0	
AlInAs	1.0×10^{18}	10.0	
AlGaInAs graded	1.0×10^{17}	40.0	Waveguide core
GaInAs	1.0×10^{17}	40.0	
AlGaInAs digitally graded	1.0×10^{17}	42.5	x25
GaInAs/AlInAs superlattice	1.0×10^{17}	42.4	
GaInAs	6.0×10^{16}	400.0	
AlGaInAs digitally graded	1.0×10^{17}	25.0	
Doped n^+ InP substrate			Waveguide cladding

Fig. 2. Schematic cross section of the complete $Al_{0.48}In_{0.52}As/Ga_{0.47}In_{0.53}As$ laser structure grown by MBE (wafer D2180). Indicated are the layers' thicknesses in nanometers and the *n*-type doping levels. Silicon was used as a dopant in all but the contact layer. The waveguide core comprises the superlattice active regions and injectors described in the caption of Fig. 1. The composition of the two 40-nm-thick AlGaInAs alloy regions is continuously varied from $Al_{0.48}In_{0.52}As$ to $Ga_{0.47}In_{0.53}As$ to smooth out heterojunction barriers under applied bias. The digitally graded AlInGaAs region adjacent to the substrate has a similar function and consists of a AlInAs/GaInAs superlattice with a 5-nm period and a varying duty factor. The laser radiation propagates parallel to the layers in the direction normal to the cleaved laser facets.

electron density must be large enough to minimize electric field penetration (depletion width) into the superlattice and space charge buildup under high current injection that would break up the minibands by means of field-induced localization (*12*). At the same time, the carrier concentration is kept low enough so that the quasi–Fermi level (E_F = 20 meV) is well below the top of the first miniband to minimize thermal occupation of these states and thus maintain a large population inversion at higher temperature. The 42.5-nm-thick injectors consist of a uniformly doped ($n = 1 \times 10^{17}$ cm^{-3}) $Al_{0.48}In_{0.52}As/Ga_{0.42}In_{0.53}As$ graded band gap superlattice alloy with constant period (5.3 nm) and varying AlInAs:GaInAs thickness ratio. When a voltage of the appropriate polarity is applied, the conduction band in the injector acquires a flat profile, and electrons are tunnel-injected into the superlattice. The onset of strong injection into the upper miniband occurs when the bottom of the miniband is approximately lined up with that of the conduction band in the injector (Fig. 1A). This onset corresponds to an applied voltage per period $\cong(\Delta_1 + E_{mg})/q$ = 0.3 V and to a total voltage U = 7.5 V, where Δ_1 is the width of miniband 1, E_{mg} is the energy of the minigap, and q is the electron charge. The latter value is in good agreement with the measured turn-on voltage of the current-voltage characteristic of the device at cryogenic temperatures (≤80 K).

The differences in waveguide refractive index between the core and claddings provide the optical confinement necessary for propagation of the radiation parallel to the layers. Calculation of the waveguide confinement factor Γ as the fraction of the optical mode in the superlattice active regions and of the effective refractive index n_{eff} of the fundamental longitudinal mode of the waveguide give Γ = 0.32 and n_{eff} = 3.21. The mode is polarized normal to the layers (TM mode), as required by the selection rule for interminiband transitions (6). The top cladding comprises a 2.4-μm-thick region of AlInAs. This large thickness is necessary because of the long wavelength (λ/n = 2.4 μm) in the material. The heavily doped 600-nm-thick GaInAs layer below the contact region achieves a high Γ and reduces waveguide losses by reducing the coupling to the plasmon mode propagating along the semiconductor-metal contact interface without requiring an AlInAs cladding layer that is too thick (*13*). The lower cladding, the InP substrate, strongly reduces the thermal impedance, compared to the use of AlInAs (*10*).

The samples were lithographically processed into mesa-etched (10 to 20 μm wide) ridge waveguides. The length of the optical cavity (L_c = 1.9 mm) was defined by cleavage of the samples. The cleaved, uncoated facets provide optical feedback. The samples, soldered to a ceramic holder, were mounted in a Helitran flow dewar. Current pulses of 70 ns at a 100 kHz were injected into the device, and the emission spectra (Fig. 3) were recorded with a Nicolet Fourier-transform IR spectrometer using a HgCdTe cooled detector. The interminiband spectra below the threshold current density $J_{th} = 8.5 \times 10^3$ A/cm^2 are broad, as expected. The dramatic narrowing and orders of magnitude increase of the optical power above J_{th} clearly demonstrates laser action. The measured longitudinal mode separation (Δ_{exp}) is in good agreement with the theoretical value [$\Delta_{th} = 1/(2nL_c)$] (Fig. 3, inset). Six devices were tested and exhibited laser action with similar spectra.

The device exhibits high optical power, which ranges from a maximum value of ≅850 mW at 5 K to ≅750 mW at 80 K (Fig. 4). The maximum operating temperature is 240 K, with an optical power as high as 30 mW. At 5 K, J_{th} = 8.5 kA/cm^2, whereas at 210 K, J_{th} = 20 kA/cm^2 (Fig. 4, inset). In the 80 to 210 K range, J_{th} can be fit with an exponential function that scales as $\exp(T/T_0)$ with T_0 = 160 K.

The threshold current density is determined by the condition

$$R \exp(\Gamma G_p - \alpha_w)L_c = 1 \qquad (1)$$

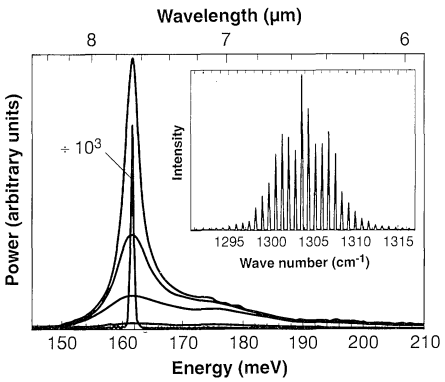

Fig. 3. Measured spectra of a laser from sample D2180. The broad spectra of the device at various bias conditions (from bottom to top, 1.48 A and 7.5 V, 1.58 A and 7.6 V, 1.69 A and 7.67 V, and 1.71 A and 7.7 V) represent the emission below threshold. The strong line narrowing and large increase of optical power observed at 1.75 A and 7.73 V (narrow curve) demonstrates laser action (the peak of this curve has been scaled down by a factor of 10^3). The laser photon energy 161 meV is in excellent agreement with the calculated value of the superlattice minigap. The radiation is polarized normal to the layers. (**Inset**) High-resolution (0.125 cm^{-1}) spectrum of the same device; the measured and calculated longitudinal mode separations Δ_{exp} and Δ_{th} are 0.786 and 0.822 cm^{-1}, respectively. The devices are ridge waveguides measuring 1.9 mm long and 10 μm wide.

where G_p is the peak material gain at threshold, α_w is the waveguide loss, and R = 0.29 is the reflectivity of the laser facets. Our calculations show that the gain spectrum peaks at the minigap energy and that G_p is given by

$$G_p = \frac{\sqrt{2\pi^3}q\mathcal{Z}_{21}^2}{\varepsilon_0 n_{eff} L_{SL} \lambda_{mg}(2\gamma)} J_{th}\tau_2 \equiv gJ_{th} \qquad (2)$$

where τ_2 = 0.9 ps is the lifetime at the bottom of the second miniband (9), L_{SL} = 42.4 nm is the superlattice thickness, ε_0 is the vacuum permittivity, and λ_{mg} is the wavelength corresponding to the minigap. The full width at half maximum ($2\gamma \cong 30$ meV) of the peak of the luminescence curve was measured at 10 K at comparable current densities in a mesa device from sample D2173 to avoid gain narrowing effects. Monolayer fluctuations in the barriers' thicknesses and donor impurity disorders determine this relatively large broadening, which we have treated as Gaussian (*7*, *14*). In deriving Eq. 2, we assumed that the electron injection efficiency into the second miniband is unity and that the injected electron distribution is thermalized at the bottom of the second miniband. The latter approximation is justified by the fact that the electrons at threshold are injected within a few tens of millielectron volts from the bottom of the second miniband and by the small intraminiband:interminiband scattering time ratio. From the threshold current density at 5 K and τ_2, we estimate a population inversion $n_s \approx 5 \times 10^{10}$ cm^{-2}.

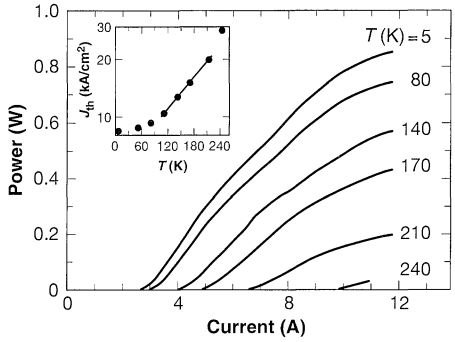

Fig. 4. Peak collected optical power from a single facet of a laser from sample D2180 as a function of bias current for various heat sink temperatures. The collection efficiency of the apparatus is ≅50%. The device is 1.9 mm long and 18 μm wide. The light from the laser was focused on an uncooled HgCdTe detector with f/1.5 optics. The pulse length is 50 ns, and the repetition rate, 4.7 kHz. (**Inset**) Measured temperature dependence of the threshold current density J_{th}. The solid line is an exponential fit, proportional to $\exp(T/T_0)$ with T_0 = 160 K. At the lowest temperature (5 K), $J_{th} = 8.5 \times 10^3$ A/cm^2.

This density corresponds to a quasi–Fermi energy of ~2 meV from the bottom of the second miniband. Thus, the width of the electron distribution is much smaller than 2γ at cryogenic temperatures.

With the aid of Eq. 2, Eq. 1 can be rewritten as

$$J_{th} = \frac{\alpha_m + \alpha_w}{g\Gamma} \quad (3)$$

where $\alpha_m = -(\ln R)/L_c = 6.5\ cm^{-1}$ is the mirror loss. We have estimated that the waveguide losses $\alpha_w = 30\ cm^{-1}$ from subthreshold spectra in continuous-wave QC lasers operating at a similar wavelength (*13*). Equation 2 then gives $J_{th} = 3.5\ kA/cm^2$, in reasonable agreement with the experimental value, considering the uncertainty in the value of the waveguide losses.

Our superlattice QC laser—along with intersubband QC lasers (*10*), cascade type-II heterostructure lasers (*15*), and InAsSb/InAlAs strained quantum-well diode lasers (*16*)—are promising mid-IR sources, alternatives to lead-salt diode lasers (*17*). We believe that the key features exploited by the present superlattice scheme—including interminiband transitions of high-oscillator strength, intrinsic population inversion, and high current capability—are particularly favorable for high optical power and long-wavelength operation (8 to 12 μm and beyond).

Note added in proof. We have recently demonstrated laser action at a wavelength of 11 μm.

REFERENCES AND NOTES

1. L. Esaki and R. Tsu, *IBM J. Res. Dev.* **14**, 61 (1970). Miniband formation was directly demonstrated in the optical experiments of R. Dingle, A. C. Gossard, and W. Wiegmann [*Phys. Rev. Lett.* **34**, 1327 (1975)].
2. F. Capasso and A. Y. Cho, *Surf. Sci.* **299–300**, 878 (1994); F. Capasso, J. Faist, C. Sirtori, *J. Math. Phys.* **37**, 14775 (1996).
3. P. Bhattacharya, *Semiconductor Optoelectronic Devices* (Prentice-Hall, Englewood Cliffs, NJ, 1994).
4. C. Waschke *et al.*, *Phys. Rev. Lett.* **70**, 3319 (1993).
5. A Kronig-Penney model with an energy-dependent effective mass m_e^* was used for the calculation of the minibands. The materials parameters are conduction band discontinuity $\Delta E_c = 0.52$eV, m_e^*(GaInAs) = $0.043m_0$, and m_e^*(AlInAs) = $0.078m_0$. Nonparabolicity was treated following C. Sirtori, F. Capasso, J. Faist, S. Scandolo, *Phys. Rev. B* **50**, 8663 (1994). The nonparabolicity coefficient is $\gamma = 1.13 \times 10^{-14}\ cm^2$.
6. M. Helm, *Semicond. Sci. Technol.* **10**, 557 (1995).
7. Electroluminescence data for samples D2135 and D2145 are reported in G. Scamarcio *et al.*, *Appl. Phys. Lett.* **70**, 1796 (1997). These wafers and D2173 have five doped superlattices interleaved with injectors and no waveguide cladding layers to suppress gain-narrowing effects on the spectra. The structures were grown on semi-insulating InP substrates wedged at 45° to collect the luminescence.
8. D. C. Herbert, *Semicond. Sci. Technol.* **3**, 101 (1988).
9. The first and second manifold of eight states of our finite eight-period superlattice were calculated. These define the first and second minibands due to the strong tunnel coupling and the broadening associated with scattering, interface roughness, and doping fluctuations. The interminiband scattering rate $1/\tau_{21}$ is calculated from the lowest state of the second miniband to the highest state of the first miniband, following R. Ferreira and G. Bastard [*Phys. Rev. B* **40**, 1074 (1989)]. The lifetime τ_2 of an electron at the bottom of the second miniband (Eq. 2) is obtained by adding the scattering rates from the bottom of the second miniband to all the states of the first miniband.
10. J. Faist *et al.*, *Science* **264**, 553 (1994). Room-temperature QC lasers are reported in J. Faist *et al.*, *Appl. Phys. Lett.* **68**, 3680 (1996); C. Sirtori *et al.*, *IEEE Photonics Technol. Lett.* **9**, 294 (1997).
11. J. Faist *et al.*, *Phys. Rev. Lett.* **76**, 411 (1996).
12. F. Beltram *et al.*, *ibid.* **64**, 3167 (1990).
13. C. Sirtori *et al.*, *Appl. Phys. Lett.* **66**, 3242 (1995); C. Sirtori *et al.*, *ibid.* **68**, 1746 (1996).
14. J. Faist *et al.*, *ibid.* **65**, 94 (1994).
15. J. I. Malin *et al.*, *ibid.* **68**, 2976 (1996).
16. H. K. Choi, G. W. Turner, H. Q. Le, *ibid.* **66**, 3543 (1995).
17. Z. Shi, M. Tacke, A. Lambrecht, H. Boetner, *ibid.*, p. 2537. For a comprehensive review of lead salt mid-IR lasers, see M. Tacke, *Infrared Phys. Technol.* **36**, 1745 (1996).

18. We are grateful to C. Gmachl for many useful discussions.

11 February 1997; accepted 21 March 1997

Spectroscopic Observation of the Formyl Cation in a Condensed Phase

Peter J. F. de Rege, John A. Gladysz,* István T. Horváth*

The formyl cation, HCO^+, has long been believed to be an important intermediate in the chemistry of carbon monoxide (CO) in acidic environments, but its spectroscopic observation in solution has been elusive. This species was generated by the reaction of CO with the liquid superacid hydrofluoric acid–antimony pentafluoride ($HF\text{-}SbF_5$) under pressure and was observed by nuclear magnetic resonance and infrared spectroscopy. Equilibria between CO in the gas phase, CO dissolved in $HF\text{-}SbF_5$, the SbF_5 adduct of formyl fluoride, and HCO^+ associated with several equilibrating anions of the type $[Sb_xF_{5x+1}]^-$ are proposed to describe the system.

Experimental observation of chemical intermediates plays a crucial role in understanding reaction mechanisms. In addition to verifying the existence of species proposed to explain known reactivity, the discovery of previously unknown intermediates can lead to dramatically different mechanistic explanations for "well-known" reactions. The isolation and identification of positively charged organic species, including carbocations, has provided a solid foundation for current understanding of organic reactions involving electrophilic species (*1*).

Protonation of weakly basic substrates to yield an activated species is central to organic transformations (*2*), enzyme catalysis (*3*), and catalysis of industrial importance (*4*). The strongest known liquid acids, such as $HF\text{-}SbF_5$ and $HSO_3F\text{-}SbF_5$, called superacids because their acidity is higher than that of 100% anhydrous H_2SO_4 (*5*), can protonate extremely weak bases (*6*), even alkanes (*7–9*). Protonation of carbonyl compounds, aromatic systems, alkenes, and many other key classes of organic species has been observed in superacidic environments (*6*, *10*). Although the chemistry of CO in acidic media is well established (*11*), the formyl cation, HCO^+, has not been observed in a condensed phase. The existence of HCO^+ has been surmised on the basis of reactions that indicate electrophilic activation of CO in superacidic media. Gatterman-Koch formylation (*11*, *12*), in which an aromatic compound reacts with CO in an acidic solution to yield an aromatic aldehyde, occurs very readily in the presence of superacids (*13–15*). The formylating agent is believed to be HCO^+ (*6*, *13–15*). The existence of HCO^+ in the gas phase has been well established by microwave, infrared (IR) (*16*), and mass (*17*) spectroscopy, and it is now recognized as one of the most abundant positive ions in deep space (*18*).

The observation of HCO^+ in superacidic solutions has been the goal of many experiments, including (i) direct protonation of CO in a variety of superacidic solutions such as $HSO_3F\text{-}SbF_5\text{-}SO_2ClF$ (*19*), $HSO_3CF_3\text{-}SbF_5\text{-}SO_2ClF$ (*13*), and $HSO_3F\text{-}Au(SO_3F)_3$ (*20*); (ii) abstraction of F^- from H(F)C=O with SbF_5 (*19*); and (iii) dehydration of formic acid (*13*, *19*). In all of these cases, CO was observed in a nonprotonated state, even when the reactions were performed at low temperatures under low CO pressure (<10 atm) to shift the protonation equilibrium (Eq. 1) to the right (*19*)

$$CO + H^+ \leftrightharpoons HCO^+ \quad (1)$$

We expected that, by increasing the partial pressure of CO (P_{CO}) above what had been used for in situ spectroscopic studies,

P. J. F. de Rege and I. T. Horváth, Corporate Research Laboratories, Exxon Research and Engineering Company, Annandale, NJ 08801, USA.
J. A. Gladysz, Department of Chemistry, University of Utah, Salt Lake City, UT 84112, USA.
*To whom correspondence should be addressed.